Omnidirectional Optical Crosslinks for CubeSats: Transmitter Optimization

Imam Uz Zaman[1], Jose E. Velazco[2], and Ozdal Boyraz[1]

[1] Department of Electrical Engineering and Computer Science, The University of California, Irvine, CA 92697, USA

[2]Jet Propulsion Laboratory, NASA, 4800 Oak Grove Drive, Pasadena, CA 91109

zamani@uci.edu, Jose.E. Velazco @ jpl.nasa.gov, oboyraz@uci.edu

Abstract— CubeSat swarm in LEO orbit is an attractive alternative to present-day expensive and bulky satellite-based remote sensing systems. This paper presents the design and optimization rules to achieve omnidirectional, high speed, long-range (more than 100 km) data communication among CubeSats. The unprecedented size, weight, power, and cost constraints imposed by the CubeSat platform and the availability of the commercial-off-the-shelf components are considered in the analyses. Analytical studies related to the scanning mirror-based beam steering system as well as scanning mirror's smallest step angle requirement are presented. In addition, we demonstrate the relations and dependencies among scanning mirror's smallest step angle, laser beam divergence, optics dimensions, communication distance, and scanning area filling efficiency, etc. Furthermore, the optimization challenges of the transmit laser beam size considering the interplay among beam divergence, beam clipping, and scattering are studied in detail. This paper also presents the effect of laser peak power, initial beam size, and communication distance on effective communication beam width to maintain a long-distance (more than 100 km) communication with SNR ≥ 10 dB at a data rate greater than 500 Mb/s.

Keywords: CubeSat, CubeSat telescope design, Free-space optical communication, Inter satellite communication, Omnidirectional optical antenna, Optical crosslink.

I. Introduction

Small satellites (e.g. CubeSat) based remote sensing technology possesses an indisputable potential to understand Earth as an integrated system and its response to natural or anthropogenic changes [1–3]. A swarm of earth-orbiting CubeSats can play a vital role in achieving small, affordable, and transformative approaches to enable remote sensing systems for wind, cloud, topography, etc. without sacrificing performance metrics that are achieved in conventional space technologies. Omnidirectional Optical Transceiver (OOT) is necessary to provide connectivity among multiple small spacecrafts to enable full-sky coverage without expensive intermediate ground relay stations as shown in Fig. 1. A seamless data transmission to the ground station is also attainable through relay nodes as long as at least one CubeSat is in the Field of View (FOV) of the ground station. Since high-speed inter-CubeSat data communication will enable data sharing among spacecrafts in the constellation, the entire swarm can perform as an unprecedented massive spaceborne remote sensing system. State of the art satellite-based remote sensing systems as discussed in Section II are bulky, use extremely large optics, consume very high power (in the order of hundreds of watts). Moreover, these satellites do not possess high speed (greater than or equal to 500 Mb/s) crosslink data transmission and data relaying capabilities. The main challenge arises from the fact that a CubeSat platform is extremely Size, Weight, Power, and Cost (SWaP-C) limited and therefore, optical system design using Commercial-off-The-Shelf (COTS) components in such a platform requires special design and optimization rules.

In this paper, we focus on the system level optics integration and design rules to achieve omnidirectional optical communication in the CubeSat platform. In our work, we investigate optical design methodologies, housing techniques,

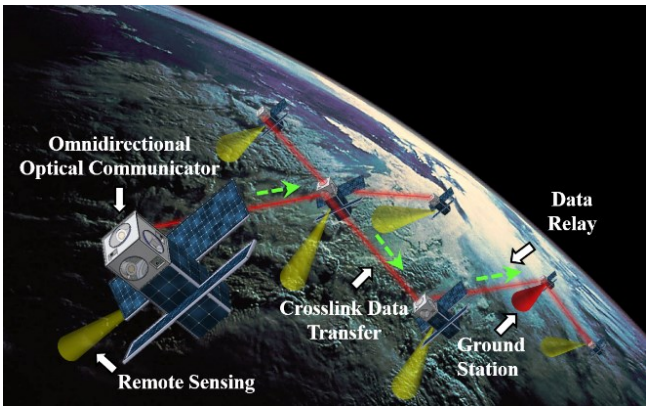

Fig. 1. CubeSat swarm interconnected by OOT.

component optimizations as well as performance tradeoffs among major COTS optical components (e.g. scanning mirrors, collimators, etc.) to address the optical system design challenges. Our OOT design goal is to achieve a blind spot free 360° Field of Regard (FOR) with maximum reach and data rate. By considering the deleterious effects such as beam divergence, satellite vibration, etc., we investigate the optimization rules for aperture size, beam width, laser power, and scanning mirror specifications to achieve design goals. Furthermore, we present the concept of Effective Communication Beam Region (ECBR) and Effective Communication Beam Width (ECBW) to address pointing accuracy challenges due to host CubeSat vibrations and receiver position uncertainties.

This paper is organized as follows: Section II briefly describes the advantage of optical communication. Section III provides the scanning mirror selection techniques based on mechanical design and FOV requirements. Section IV formulates the small step angle requirement of the scanning mirror and filling efficiency. In Section V, we present the transmitter beam size optimization based on scanning mirror size, ECBR, ECBW, and receiver position uncertainty followed by a conclusion.

II. The Advantage of Optical Crosslink and State of The Art Satellite-Based Remote Sensing

Modern wireless inter-satellite communications are mostly based on RF and microwave technologies. Recent progress in the microwave-based CubeSat communication systems demonstrates a high data rate (up to 1.6 Gb/s) point to point communication [4,5]. The versatile deployment of microwave technologies for simultaneous communication between multiple satellites in the CubeSat platform is limited by the bandwidth and the antenna size requirement. Optical transceivers have the potential to provide an order of magnitude improvement in data transmission capacity over the microwave counterpart with a significantly smaller form factor than that of microwave systems [6]. However, omnidirectional (one-to-many) high-speed cross-link data communication and data relaying capability in a CubeSat platform are still open for investigation in the optical domain [7]. Optical transceivers

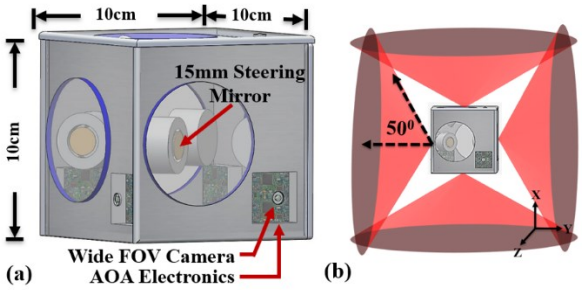

Fig. 2. (a) A CubeSat omnidirectional optical communicator (b) The concept of 360° field of regard.

present a high data rate by taking advantage of their several orders of magnitude shorter wavelengths that lead to a very narrow transmit beam or a very directive antenna. The received optical power (P_{rcv}) at a distance R can be represented as, $P_{rcv} = P_T G_T G_R L L_R L_T L_P \sigma_T \sigma_R$. Here, P_{rcv}, P_T, G_T, G_R, L, L_R, L_T, L_P, σ_T, σ_R represent received power, transmit power, transmit antenna gain, receive antenna gain, path loss, receiver plumbing loss, transmitter feeder loss, pointing loss, transmitter efficiency, and receiver efficiency, respectively. Moreover, the transmitter antenna gain $G_T = \left(\frac{\pi D_T}{\lambda}\right)^2$, and receiver antenna gain $G_R = \left(\frac{\pi D_R}{\lambda}\right)^2$ reveals the $1/\lambda^2$ dependence of the received power. This makes the optical regime more attractive than the microwave regime. Furthermore, optical transceivers provide very low beam divergence ($\theta \approx \lambda / D_T$), high wideband communication channel, and very high immunity to interference. However, establishing and maintaining a point to point optical link between two moving satellites is a tough task and therefore requires an advanced Attitude Determination and Control System (ADCS) for proper pointing, acquisition, and tracking. State of the art satellite-based remote sensing systems such as CALIPSO (launched in 2006) [8], TwiLiTE [9], are extremely expensive to deploy and difficult to maintain.

Up to date, several optical communication methods have been explored for mini and microsatellites [10–12]. The optical communication between CubeSats is a relatively new area of research and development [12–14]. To the best of the authors' knowledge, all the research and development work on the satellite optical links such as Low Earth orbit (LEO) to LEO and LEO to Earth have been done either for satellites with significantly less SWaP-C constraints or a single point-to-point data communication link. Additionally, the omnidirectional optical system in CubeSat is a new and demanding concept that possesses its unique design challenges. To establish high-speed optical connectivity among different CubeSats in the constellation, the optical communicator must possess full FOR, high scanning rate, fast Angle of Arrival (AOA) detection system as well as capability to maintain multiple communication links simultaneously. These requirements impose unique design challenges that need to be addressed. We briefly presented the design tradeoffs and challenges to achieve high speed omnidirectional optical antenna [15,16]. In this paper, we provide an in-depth analysis of the transmitter optics integration and design methods to enable omnidirectional optical communication in the CubeSat platform.

A small, cost-effective omnidirectional optical communicator can be fabricated using multiple transceiver apertures as in Fig. 2 (a). Each face of the CubeSat is equipped with one scanning mirror-based transceiver that possesses an optical scanning up to ±50°. Therefore, a total of six transceiver units need to be integrated to achieve a 360° FOR as illustrated in Fig. 2(b). The coverage in the Z-axis is not shown for the sake of picture clarity. A technological concept of a Low Earth Orbit (LEO) formation flying (Q4) incorporating such an omnidirectional optical cross-link had been presented before [2,7].

This article has been accepted for publication in a future issue of this journal, but has not been fully edited. Content may change prior to final publication. Citation information: DOI 10.1109/TAES.2020.2995320, IEEE Transactions on Aerospace and Electronic Systems

III. Transmitter Design Tradeoffs and Sample Link Budget

To establish a free space optical link effectively, an advanced spatial acquisition and pointing system must be incorporated in the Omnidirectional Optical Transceiver (OOT). A Scanning Mirror (SM) is the foremost component in the optical pointing system. A high-speed, wide-angle scanning mirror is desirable for a fast scanning and pointing mechanism. However, the scanning capability of the SM is intertwined with its size, form factor, and driving mechanism. In a non-mechanical beam steering system (e.g. a MEMS-based, a dual-axis vector mirror-based), the scanning frequency decreases drastically with the increase of mirror size. For example, the current state of the art 0.8 mm diameter MEMS mirror from a reputed vendor has a resonant frequency approximately at 4 kHz, whereas a 2.00 mm diameter MEMS mirror shows a resonance at 1.3 kHz [17]. A relatively large scanning mirror (e.g. 15 mm) offers a scanning speed of up to 350 Hz [18]. Additionally, the mirror dimension and driving mechanism determine the maximum achievable scanning angle. For instance, commercially available high-speed MEMS mirrors have a diameter of 0.8 mm to 7.5 mm with a mechanical scanning angle of less than ±7°. On the contrary, relatively slow dual-axis vector scanning mirrors (5 mm to 16.5 mm) have mechanical scanning of about ±25° as in Fig. 2. Therefore, the scanning mirror needs to be selected considering the interplay between mirror size, mirror speed, scanning angle, and form factor.

In the far-field ($R \gg Rayleigh\ range$), the full divergence angle, 2δ ($1/e^2$ diffraction angle) of a Gaussian beam is assumed to be constant. The divergence angle is inversely proportional to the initial beam waist (ω_o) and also proportional to the wavelength (λ), and beam quality factor M^2 as described in[19,20], $2\delta \approx M^2 \frac{2\lambda}{\pi\omega_o}$. Since deviations from the Gaussian beam requires a detailed discussion of specific beam profiles and possible laser modes, a Gaussian beam with $M^2 \approx 1$ is assumed in all analyses presented in this paper. In many applications, the scanning mirror's diameter (D_m) limits the allowable transmit beamwidth (D_T), $D_T < D_m$. Obviously, incorporating a beam expander after the scanning mirror might seem to be a functional way to achieve a larger transmit beam waist than the scanning mirror size as presented in Fig. 3.

Fig. 3(a) and Fig. 3(b) shows the scanning mechanisms incorporating a Galilean beam expander and a Keplerian beam expander, respectively. The collimated beam is first steered by the scanning mirror that creates an angle, θ_{in} at the input of the beam expander as can be seen from Fig. 3. The beam is expanded by a beam expander and finally makes an angle of θ_{out} at the output aperture.

The Galilean beam expander is comprised of a concave lens (CC) and a convex lens (CV) with focal lengths of FL_1 (-ve) and FL_2 (+ve), respectively as shown in Fig. 3(a). The Keplerian beam expander incorporates two convex lenses with focal lengths of FL_1 (+ve) and FL_2 (+ve) as presented in Fig. 3(b). Both beam expander systems can be represented by

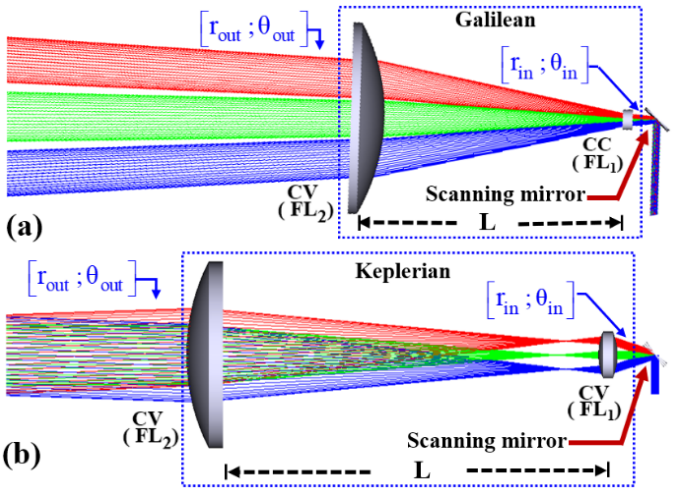

Fig. 3. Free space optical transmitter, (a) Galilean beam expander-based system and (b) Keplerian beam expander-based system.

renowned ABCD ray matrix:$[r_{out}; \theta_{out}] = [A \quad B; C \quad D][r_{in}; \theta_{in}]$. Here, r and θ correspond to the ray position and the ray angle. A= $\delta r_{out}/\delta r_{in}$, $B = \delta r_{out}/\delta\theta_{in}$, $C = \delta\theta_{out}/\delta r_{in}$, and $D = \delta\theta_{out}/\delta\theta_{in}$ represent spatial magnification, angle to position mapping, position to angle mapping, and angular magnification, respectively. The ABCD matrix of both Keplerian and Galilean telescope can be given as

$$[A\ B; C\ D] = \left[1 - \frac{L}{FL_1} \quad L; \frac{L - FL_1 - FL_2}{FL_1 \cdot FL_2} \quad 1 - \frac{L}{FL_2}\right]$$

The beam expanders are afocal systems, therefore $L = FL_1 + FL_2$. It is evident from the ABCD matrix that the spatial magnification for both telescopes is $\left|-FL_2/FL_1\right|$, whereas the angular magnification is $\left|-FL_1/FL_2\right|$. Hence, a beam expander-based transmitter reduces the scanning angle by the same factor as it expands the beam size. For example, if a scanning mirror is capable of optical scanning $\theta = \pm 30^o$, incorporating a 3X beam expander (as shown in Fig. 3) decreases the scanning range to about $\pm 10^o$. Since the reduction in beam scanning angle, as presented in ABCD matrix calculation, is not suitable for OOT design, there is no need for detailed beam analysis and discussion of the nonlinear distortions that are missing in the ABCD matrix analysis. The scanning range at the output aperture of the transceiver also determines the required number n of the transmitter branches (defined as the required set of optical components to transmit data) to achieve an omnidirectional coverage, and it is estimated by, $n = ceiling\left(\left(\frac{\sin(\pi\alpha_{rec}/720)}{\sin(\pi\alpha_{mec}/360)}\right)^2\right)$. In this equation, α_{rec} is the required field of view (full angle) and α_{mec} is the steering mirror's mechanical full scanning range. Optical scanning angle, $\theta = 2\alpha_{mec}$. Using the equation, it can be estimated that 15, 9, and 6 independent transmitter branches are required to achieve a full field of view (360°) by incorporating a scanning

This article has been accepted for publication in a future issue of this journal, but has not been fully edited. Content may change prior to final publication. Citation information: DOI 10.1109/TAES.2020.2995320, IEEE Transactions on Aerospace and Electronic Systems

mirror with 30°, 40°, and 50° full mechanical scanning ranges, respectively.

Considering the tradeoffs of the scanning mirror parameters, a simple and compact transmitter design concept utilizing a single collimating aspheric lens and a small MEMS mirror is shown in Fig. 4(a). The Fixed Mirror (FM) is mounted at angle γ (degree) so that the horizontal collimated beam makes an Angle of Incidence (AOI) of β on the SM as shown in Fig. 4(a). Given that the SM is mounted at 45° w.r.t. the vertical axis in the example type A design, the AOI can be expressed as, $\beta = 135 - 2\gamma$. The allowable AOI (less than or equal to 22.5°) is enforced by the projected shape of the SM from the collimated beam's perspective, and the anti-reflection coating at the aperture window. Fig. 4(b) presents the required distance between two mirrors ρ for different scanning angles and AOI. The required transmitter diameter (TD) increases with the increase of the scanning angle of the SM for a given AOI that is also shown in Fig 4(b). To illustrate, for the given system design with transmitting beam diameter =3.8 mm, fixed mirror diameter =5.0 mm, scanning mirror diameter =6.0 mm, and TD ≤ 20 mm, it can be calculated that the maximum scanning angles are 8°, 7.2°, and 5.8° for AOI (β) of 22.5°, 20°, and 17.5°, respectively. It can also be realized that for a given AOI, a large scanning angle requires a large TD and a larger ρ which make the omnidirectional transmitter design challenging due to CubeSat volume constraint. Additionally, due to a small transmit aperture, type A transmitter design requires an independent transmitter aperture and receiver aperture.

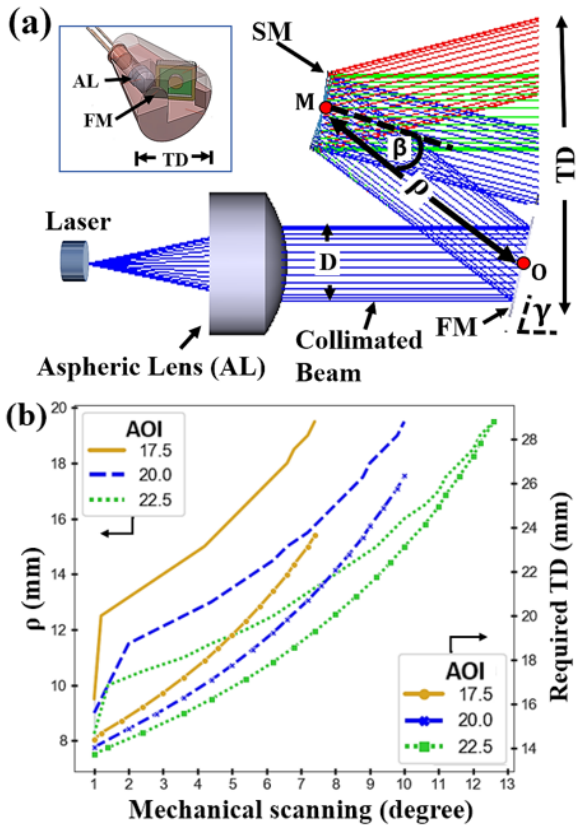

Fig. 4. (a) Type A transmitter design, (b) the required ρ and TD for different scanning angles.

A second design approach (Type B) can manifest a smaller form factor when the mirrors have a large diameter (e.g. 10 mm) and wide mechanical beam scanning angle (e.g. ±25°) as shown in Fig. 5. Type B transmitter can be transformed into a complete wavelength selective optical transceiver with very low crosstalk (close to 0%) and low optical power loss (about 3 dB) [15]. Due to a larger mirror size compared to type A design, this design approach allows the same aperture to be used as a transmitter and as a receiver aperture. Therefore, once the communication link is established, this transceiver design approach ensures a direct line of sight communication among multiple nodes. Type B design also evades the design difficulties related to ultra-wide FOV receiver design. The transmitter branch of type B transceiver consists of a fixed mirror (FM), a dichroic filer (DF), and a scanning mirror (SM) as shown in Fig. 5. A Focusing Lens (FL) focuses the received optical signal on a Photo Detector (PD) e.g. Avalanche PhotoDiode (APD). A small fraction (about 5%) of the received signal is sampled by a beam sampler (S) and focused on the Quadrant Detector (QD) to generate a feedback signal for SM. This compact design approach also allows us to install up to six transmitter branches in less than 3U that are required to achieve omnidirectional data communication as shown in Fig. 2.

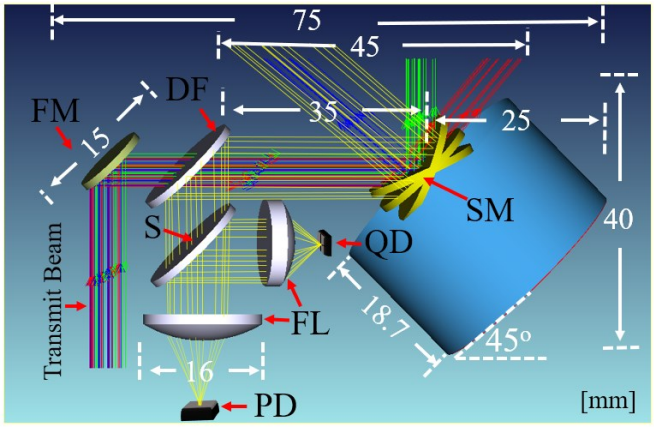

Fig. 5. Type B transmitter design in Zemax. All dimensions are in millimeters.

An example link budget that can achieve more than 600 Mb/s data rate up to 100 km communication distance by incorporating a high-speed 15 mm transceiver aperture is presented in Table I. The data rate R_b is estimated from the bandwidth (B), the received power (P_{rcv}), bit energy (E_b), link margin (M), and noise density (N_o), $P_{rcv}/N_o = E_b/N_o + R_b + M$. Here all the terms are in dB. State-of-the-art Forward Error Correction (FEC) schemes e.g. RS(255,239), RS (255, 191), etc., require pre-FEC Bit Error Rate (BER), $BER_{pre-FEC} \leq 4 \times 10^{-3}$ to attain post-FEC BER, $BER_{post-FEC} \leq 5 \times 10^{-15}$ [21,22]. The required E_B/N_o ratio to achieve the FEC limit is about 11.2 dB, 8.5 dB, and 20.5 dB for On-Off Keying (OOK), Binary Phase Shift Keying (BPSK), and Pulse Position Modulation-2 (PPM-2), respectively

TABLE I
OPTICAL COMMUNICATION LINK BUDGET

Wavelength	850 nm	
Modulation format	OOK	
Transmit power (1 W)	30 dBm	
Transmitter aperture gain (10 mm)	91.4 dB	
Receiver aperture gain (15 mm)	94.8 dB	
Path loss (100 Km)	-243.4 dB	
Transmitter and Receiver loss	- 3.0 dB	
Spatial pointing loss, Lp	3 dB 8.6 dB (pointing error=δ)	
Received power	-33.16 dBm -38.76 dBm	(Lp = 3.0 dB) (Lp = 8.6 dB)
Receiver sensitivity (1 GHz APD)	-50 dBm	
Receiver noise figure	-4.0 dB	
Link margin	3 dB	
Estimated data rate	615 Mb/s 170 Mb/s	(Lp = 3.0 dB) (Lp = 8.6 dB)

IV. MIRROR SMALL STEP SIZE REQUIREMENT

Scanning mirror's maximum scan range determines the attainable Field of Regard (FOR) and the required number of transmitter branches. However, the mirror's Smallest Step Angle (SSA) determines the transmitter's ability to point at a certain direction inside the scanning area to establish communication links and to maintain seamless communication in a constellation. Hence, the required scanning mirror's smallest step angle needs to be determined carefully.

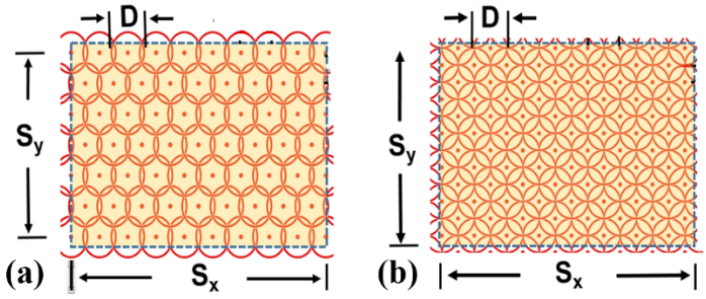

Fig. 6. Scanning area filling pattern (a) HFP, (b) SFP.

Quasi-static scanning mode (point-by-point scanning) is considered in our analysis to derive the mirror's required SSA. In quasi-static mode, two filling patterns can be used to scan a scanning area efficiently: Hexagonal Filling Pattern (HFP) and Square Filling Pattern (SFP) as shown in Fig. 6 where S_X and S_Y are horizontal and vertical scanning range of the scanning mirror. Besides, D represents the transmit beam diameter at the scanning area and each dot (.) represents a single pointing point (transmit beam center) on the scanning area. The number of the required minimum scanning points (N) in quasi-static mode to fill an area A can be approximated by,

$$N \approx \left(8/3\sqrt{3}\right)\left({S_x S_y}/{D^2}\right) \quad for\ HFP \qquad (1)$$

$$N \approx 2\left({S_x S_y}/{D^2}\right) \quad for\ SFP \qquad (2)$$

It can be seen that HFP requires a smaller number of scanning points to fill the scanning area and therefore requires less time to scan in the quasi-static scanning mode. In the SSA analysis, a rectangular scanning area at a distance R from the optical transmitter is assumed as presented in Fig. 7. Considering, R>>Rayleigh range the beam diameter at R can be expressed as

$$D \approx D_o + 2R\tan\delta \qquad (3)$$

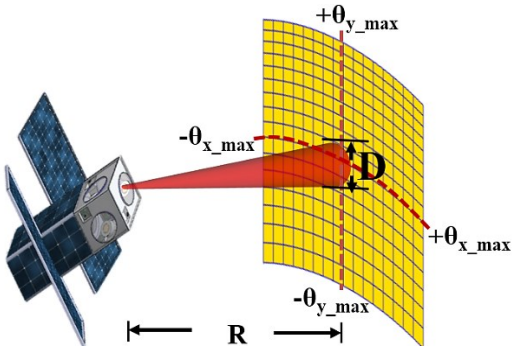

Fig. 7. CubeSat scanning area.

Here, D_o and δ are initial beam diameter and half divergence angle. Considering the above-mentioned parameters, scanning mirrors the smallest step mechanical angle α is calculated. The calculated scanning mirror's SSA requirements for HFP and SFP scanning pattern can be approximated as

$$HFP: \alpha_x \le \frac{1}{2}\tan^{-1}\left(\frac{\sqrt{3}D}{2R}\right) \ and\ \alpha_y \le \frac{1}{2}\tan^{-1}\left(\frac{3D}{4R}\right) \qquad (4)$$

$$SFP: \alpha_x \le \frac{1}{2}\tan^{-1}\left(\frac{D}{R}\right) \ and\ \alpha_y \le \frac{1}{2}\tan^{-1}\left(\frac{D}{2R}\right) \qquad (5)$$

Here α_x and α_y are the required SSA for X and Y axes scanning, respectively. For most inter-satellite data communication, $R >> D$. As a result, (3) can be approximated as, $D \approx 2R\tan\delta$. Considering long-distance communication, the SSA for HFP and SFP can be expressed as

$$HFP: \alpha_x \le \frac{1}{2}\tan^{-1}\left(\sqrt{3}\tan\delta\right), \alpha_y \le \frac{1}{2}\tan^{-1}\left(\frac{3}{2}\tan\delta\right) \qquad (6)$$

$$SFP: \alpha_x \le \frac{1}{2}\tan^{-1}(2\tan\delta), \alpha_y \le \frac{1}{2}\tan^{-1}(\tan\delta) \qquad (7)$$

It is obvious from (6) and (7) that the smallest step angle requirement to achieve blind-spot free scanning is independent of the communication distance R and depends solely on the divergence angle δ in a long-range data communication. Note that, we define blind spots as the area where the transmitter is unable to point the transmit beam inside its scanning area. Most of the commercially available scanning mirrors possess the same step angle for both axes. As a result, a scanning mirror must be selected such as the smallest step mechanical angle, $\alpha \le min\ (\alpha_{x\_u}, \alpha_{y\_u})$ to ensure full scanning area coverage. Here, α_{x_u} and α_{y_u} are the upper bound of the required mechanical SSA for X and Y axes, respectively. Otherwise, the optical transmitter contains a blind spot inside the scanning

This article has been accepted for publication in a future issue of this journal, but has not been fully edited. Content may change prior to final publication. Citation information: DOI 10.1109/TAES.2020.2995320, IEEE Transactions on Aerospace and Electronic Systems

range. In our analysis, the transmitter beam size and the

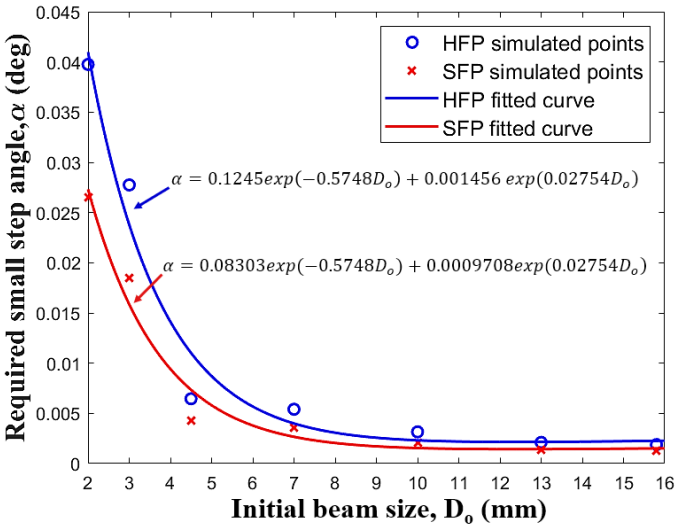

Fig. 8. Required mechanical small step angle of the scanning mirror. The solid lines are the nonlinear least-square fit on simulated data points.

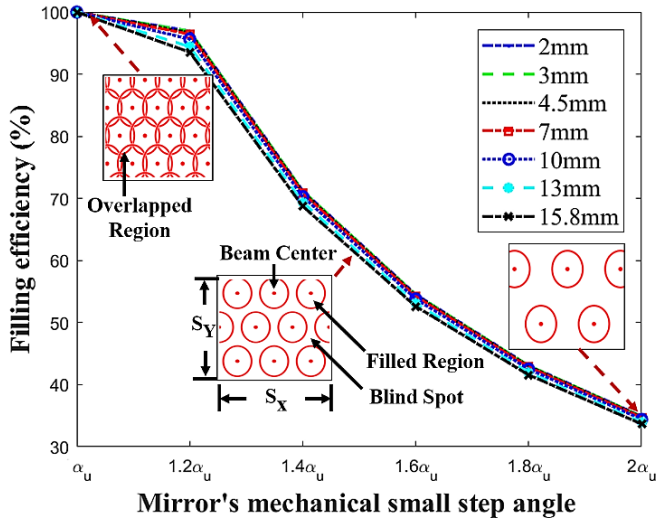

Fig. 9. Scanning area filling efficiency for different initial beam sizes and small step angles.

corresponding divergence data are incorporated from commercially available optical collimators [23–25]. The transmitter beam size and half divergence angle data are summarized in Table II. Using the transmit beam data provided in Table II, we find the minimum step angle requirement of the scanning mirror for both Hexagonal and Square filling patterns using (6) and (7), respectively. The upper bound of the required SSA is shown in Fig. 8. The required small step angle can be approximated by the fitted models shown in Fig. 8. The fitted models of the smallest step angle for HFP and SFP are also included in Fig. 8.

Evidently, HFP relaxes the SSA requirement more than SFP. The difference in the required α is noticeable at a smaller

TABLE II
BEAM DIVERGENCE

Beam Diameter (mm)	Divergence Angle (deg)	Beam Diameter (mm)	Divergence Angle (deg)
2.1	0.053	7.0	0.0072
3.0	0.038	10.0	0.0042
3.6	0.016	13.0	0.0028
4.5	0.0086	15.8	0.0025
5.5	0.0077	16.5	0.0023

transmit beam. For instance, a 2 mm initial beam requires $\alpha \leq 0.0398^o$ and $\alpha \leq 0.0265^o$ for HFP and SFP, respectively. For a large initial beam such as 13mm transmit beam the required $\alpha \leq 0.00021^o$ and $\alpha \leq 0.0014^o$ for HFP and SFP respectively. If the scanning mirror fails to possess the required SSA, we need to determine the scanning area filling efficiency of the selected scanning mirror. It is evident from (1), (2), and Fig. 8 that HFP is a more effective scanning pattern than SFP in terms of scanning time (number of required scanning points) and SSA requirement. Hence, we consider HFP for the filling efficiency calculation to demonstrate the concept. Moreover, to simplify the mathematical formulation of the created blind spot inside the scanning area due to the mechanical smallest step angle, in our analysis, we assume a square scanning area ($S_X = S_Y$), $\alpha_x = \alpha_y$, circular laser beam, and equal optical scanning range in both axes. The filling efficiency of the HFP can be written as

Here Ω and δ are the mechanical SSA of the scanning mirror and the beam divergence angle, respectively. In our algorithm, the FE is set to 100% for $\Omega \leq \alpha_u$ where α_u is the upper limit of the required scanning mirror's smallest step mechanical angle(α). For example, in HFP the actual area filled by the 2 mm scanning beam at $\Omega = \alpha_u$ is about 140% due to the overlapped regions as in Fig. 9, which is set to 100%. Using (8), the filling efficiency as a function of the upper bound of the mirror's required smallest step angle α_u for different initial beam size is calculated and shown in Fig. 9. It can be seen that the filling efficiency drops to about 35% for all transmit beam size if the mirrors SSA is twice than the upper bound of the required small step angle.

V. TRANSMIT BEAM SIZE OPTIMIZATION

A. Initial Beam Diameter to Mirror Diameter Ratio

Initial beam size needs to be optimized considering the available scanning mirror parameters (size, scanning speed, frequency) and far-field beam characteristics such as peak irradiance, beam size, etc. The peak irradiance at the far-field can be defined as, $I_{peak} = \frac{2P_o}{\pi\omega^2}$ where P_o, ω represent the total power and the beam waist, respectively at a certain distance [19]. The received power at the receiver, $P_{rcv} = Intensity \times A_{rec}$ where A_{rec} is the area of the receiver aperture. It is quite common to utilize the scanning mirror as the transmitter and receiver aperture to ensure a wide scanning angle as discussed in section III(B) as well as a wide field of view receiving capability. As a result, the relative size between

This article has been accepted for publication in a future issue of this journal, but has not been fully edited. Content may change prior to final publication. Citation information: DOI 10.1109/TAES.2020.2995320, IEEE Transactions on Aerospace and Electronic Systems

the transmit beam diameter D_T and the scanning mirror diameter D_S plays an important role in optimizing the far-field beam profile, beam size, scanning resolution, and peak intensity. Furthermore, the ratio, $M_R = D_T / D_S$ needs to be optimized considering the tradeoffs among divergence, scattering and beam clipping at the mirror aperture. The

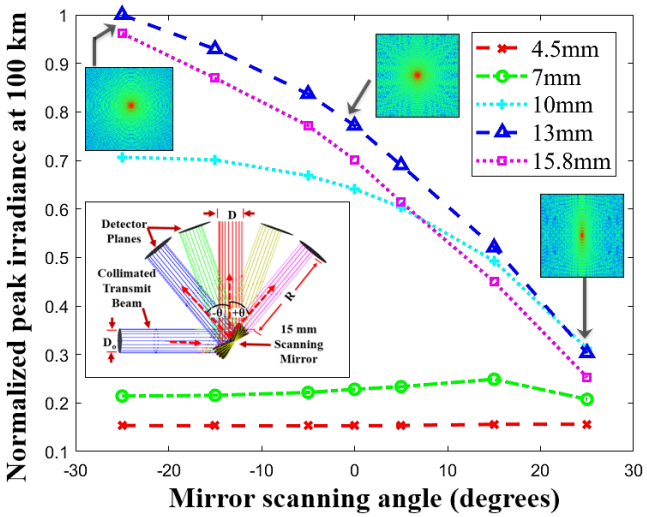

Fig. 11. Effect of the mirror's instantaneous angle on the peak irradiance.

collimated laser beam can be optimized to under-fill ($M_R < 100$ %) or over-fill ($MR \geq 100$ %) the scanning mirror. It is seen from Fig. 10 that an overfilled Gaussian beam can exhibit less divergence and therefore smaller beam size at the target. Three fast mirrors (15 mm, 10 mm, and 5.5 mm) are used in the Zemax simulation.

We estimate that the far-field beam radius decreases from 110 m to 20 m approximately for a 5.5 mm beam as M_R increases from 20% to 90%. Beam size in Fig. 10 is measured as $1/e^2$ radius at a 100 km distance. However, when the beam size is comparable to mirror size it experiences higher beam profile distortion due to the scattering and diffraction phenomena. Additionally, it can be seen that the peak irradiance also increases up to a certain M_R and reaches a maximum when $80\% \leq M_R \leq 90\%$ as shown in the figure. Fig. 10 is created considering a 0^o scanning angle of the scanning mirror. The dependence of the peak irradiance on the mirror's instantaneous scanning angle is discussed in the following section. Three commercially available compact scanning mirrors (15 mm, 10 mm, and 5.5 mm [17,18]) are placed in the place of SM as shown in Fig. 5 in the beam radius and irradiance simulation as shown in Fig. 10. Moreover, the beam divergence data is incorporated from Table II.

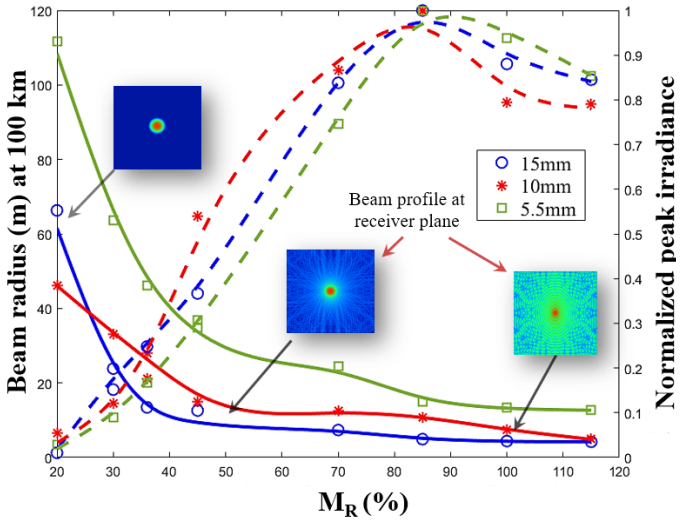

Fig. 10. Effect of M_R on the beam size (solid curves) and peak irradiance (dashed curves) at 100 km.

B. *Beam Optimization Considering Scanning Angle*

A large scanning angle (greater than 10^o) is desirable in a small form factor as shown in Fig. 2 and Fig. 5. However, when the beam size and the mirror size are comparable, the mirror scanning angle affects the intensity profile at the far-field and therefore causes scanning angle-dependent received power variation. As a proof of concept, peak irradiance variation due to different scanning angles at a 100 km distance for different initial beam sizes are presented in Fig. 11.

Here, we consider a laser peak power of 1 W and the scanning mirror is mounted at 45^o w.r.t the optical path as shown in Fig. 11 (inset). A 15 mm mirror with a large scanning range ($\pm 25^o$ mechanical scanning) is considered for this analysis. The vertical axis is the peak irradiance normalized to the peak irradiance of a 13 mm transmitter beam as it shows the maximum peak irradiance at the far-field. It can be observed from Fig. 11 that the peak intensity varies noticeably if the laser beam diameter ($1/e^2$) is greater than 30% of the diameter of the scanning mirror. For example, at a large scanning angle, the peak irradiance can drop to about 10% and about 70% for a 7 mm and 13 mm laser beam, respectively as shown in Fig. 11. It can also be seen from Fig. 10 (insets) that the intensity profile gets distorted from the ideal profile (Gaussian profile) based on ratio, M_R. A relatively large beam (w.r.t. mirror diameter) manifests high peak intensity due to low divergence, nevertheless, the beam shape distortion is higher for a larger beam. Moreover, the far-field beam intensity profile also varies with the scanning mirror's instantaneous scanning angle due to the beam clipping and the scattering phenomena. For example, the beam profile variation in the far-field (100 km away from the transmitter) for a 13 mm initial beam size and different scanning angle is shown in Fig. 11(insets). As a result, the transmit beam size for CubeSat for a given scanning mirror

should be optimized considering the interplay between the divergence and the diffraction of the transmitter beam.

C. Beam Optimization Considering Pointing Challenges.

The uncertainty of the satellite position leads to the challenges in the pointing accuracy that must be considered in the designing of a CubeSat optical transmitter. The transmitted laser beam width needs to be optimized considering the position uncertainty and the imperfect knowledge of the CubeSat orientation[26,27]. At a fixed scanning angle, due to the Gaussian beam profile of the transmitted beam, the error-free data communication is possible only if the receiver falls into a small region of the beam where the beam intensity is high enough to maintain desired SNR. Two figures of merit, Effective Communication Beam Region (ECBR) and Effective Communication Beam Width (ECBW) are introduced to quantify the initial beam size optimization technique considering pointing and tracking challenges inherited by optical communication. The Effective Communication Beam Region (ECBR) can be defined as the approximate circular area in the 2D space of the transmitted beam at a target within which a receiving CubeSat can maintain a desired SNR e.g. greater than 10 dB. The ECBW is the diameter of this ECBR. Once the pointing and acquisition are completed with the state-of-the-art methods (as suggested in [27–29]), ECBR and ECBW can be used to quantify the immunity of the communication link from the random angular disturbance. The pointing of the transmitted beam needs to be just accurate so that the receiving CubeSat lies inside the ECBR. A system designed to have a large ECBR relaxes the pointing and tracking challenges compared to the system that possesses small ECBR. Therefore, a larger ECBR manifests higher robustness to random CubeSat vibrations and position uncertainties. Considering Gaussian beam profile, the received optical power at the receiver varies as $P_{rcv}(d,R) = I(d,R) \times A_{rec}$ where $I(d,R) = \frac{2P_R}{\pi[r(R)]^2}\exp\left(\frac{-2d^2}{[r(R)]^2}\right)$, d, R, $r(R)$, and P_R are the intensity distribution in the 2D plane, receiver position from the transmit beam center, communication distance, beam radius ($1/e^2$) at distance R (as in section VA), and total optical power at the receiver plane, respectively [19]. Under the assumption of negligible power loss in the space, $P_R \approx P_T$,. The data communication link is effective if the received power is greater than or equal to the required power, $P_{rcv}(d,R) \geq P_{req}$. The required average optical power, $P_{req} \geq \sqrt{(SNR_{req} \cdot \sigma^2)/(R_p^2 \cdot M^2)}$, here, SNR_{req}, σ^2, M, R_p refer to the required SNR, total noise power, the APD gain, and the photodiode responsivity, respectively. ECBW is defined as, $P_{rcv}\left(\frac{ECBW}{2}, R\right) = P_{req}$. Given the above-mentioned conditions, the ECBW can be derived as

$$ECBW = \sqrt{2\,r(R)^2 \cdot ln\left(\frac{2\,P_T\,R_a^2}{P_{req}\,r(R)^2}\right)} \qquad (9)$$

In the free-space optical communication link, the ECBW is very effective as it is directly related to SNR and therefore, the data rate of the communication link. CubeSats C1, C2, and C4 in Fig. 12(inset) can achieve $SNR \geq 10$ dB because they are inside the ECBR. However, data communication cannot be established with C3 due to the low SNR. The Zemax beam propagation simulation of the received power by a 15 mm receiver lens for different positions (relative to the transmit beam center) of the receiving CubeSats at a 100 km distance is shown in Fig. 12. Four different initial beam sizes (4.5 mm, 7 mm, 10 mm, and 13 mm) and three normalized SNR levels are considered for the illustration. All powers in Fig. 12 are normalized to the received power of a 13 mm transmit beam. It can be observed that the ECBW for 13 mm, 10 mm, 7 mm, and 4.5 mm are about 14 m, 17.3 m, 22 m, and 26.29 m, respectively. Due to the small receiving aperture (15 mm) and high divergence, a high peak transmit power (about 10 W) is required to achieve an acceptable SNR at long distance (e.g.100 km) for relatively smaller transmit beam size e.g. 4.5 mm and 7 mm. Therefore, for the sake of comparative analysis and visualization, we assume a 10 W peak transmit power in Fig. 12.

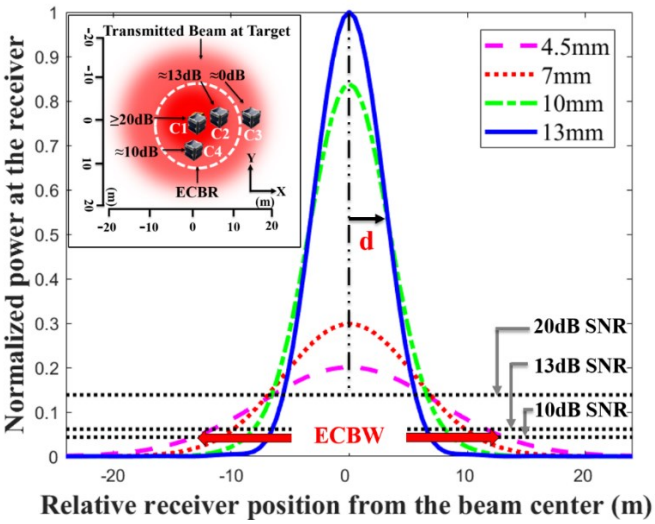

Fig.12. Effect of the relative receiver position from the transmit beam center on normalized received power.

Given a laser with average power P_{AVG}, infinite extinction ratio, and duty cycle D, the theoretical attainable peak power (P_{peak}) of a laser can be estimated as, $P_{peak} > P_{AVG}/D$. For instance, a laser operating at a 5% duty cycle and a 0.5 W average power can generate pulses with more than 10 W peak power. Up to date, several laser technologies have been demonstrated and they can provide several Watts to kilo Watts of peak power [28,30–32]. Therefore, a 10 W peak power is indeed achievable by optimizing the laser modalities and the extinction ratio of the incorporated COTS lasers and amplifiers. Fig. 13 summarizes the simulation results of the free space optical link to estimate ECBW for different initial beam sizes and powers over various distances. In short distance communication (less than 10 km), the ECBW for all transmit beam sizes are close to each other (in the range of 2 m to 6 m) for any transmitted beam size due to the negligible effect of the divergence. However, the effect of the initial beam size is notable in long-distance communication (beyond 50 km). For example, given that the initial peak power 10 W, at a 50 km communication distance the ECBW is measured as 18 m, 11.5

This article has been accepted for publication in a future issue of this journal, but has not been fully edited. Content may change prior to final publication. Citation information: DOI 10.1109/TAES.2020.2995320, IEEE Transactions on Aerospace and Electronic Systems

m, and 7.6m for 4.5mm, 10 mm, and 13 mm transmitted beam, respectively. It can be observed the ECBW of 4.5 mm beam gradually goes to zero as communication distance increases due to the lack of power to maintain a 10 dB SNR link.

Furthermore, it can also be seen from Fig. 13 that the effect of transmitter beam size on ECBW is more prominent if the laser peak power is increased (a commonly adopted technique[33]) to achieve long-distance communication. For instance, at 100 km communication distance, a 10 mm transmit beam manifests ECBW of 8.58 m and 17.3 m for 1 W and 10 W peak power respectively. Although the results presented here are the Zemax simulation results for higher accuracy, the presented (9) can be used to get a closer estimation of ECBW.

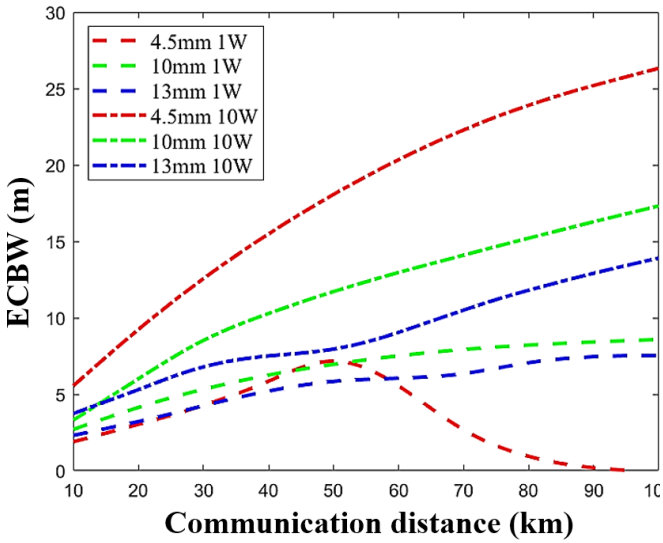

Fig. 13. Effect of transmitter peak power on ECBW at different communication distances.

D. Feasibility Study of the Pointing Accuracy

From the sample ECBW calculation described in the previous section, the estimated required pointing accuracies at 100 km communication distance are less than 0.004°, 0.005°, 0.006°, and 0.0075° for 13 mm, 10 mm, 7 mm, and 4.5 mm transmit beam diameters, respectively. Recent advances in star tracking technologies, as well as scanning mirror technologies, demonstrate a higher pointing accuracy than the required pointing accuracy. For instance, an advanced star tracker demonstrates a pointing accuracy of ±0.003° [34]. Recent advances in MEMS scanning mirrors (e.g. Mirrorcle [17]) reveal mirror actuators of greater than 14 bits (16384 positions) on each axis. Therefore, the MEMS mirrors with a mechanical tilt range of -7° to +7° on each axis present a tilt resolution less than 0.0008° (or smaller than 14μrad) on both axes. The dual axis vector mirror (e.g. Optotune [18]) with ±25° mechanical scanning capability claims to possess a closed loop resolution less than $5\,\mu rad$. In the type B transceiver design, alongside the star tracker of the host satellite, each transceiver is equipped with a high-speed camera based coarse Angle of Arrival (AOA) detection system as shown in Fig. 2. In addition, the Quad Detector (QD) as shown in Fig. 5 facilitate the fine pointing and tracking mechanism for the Scanning Mirror. We believe that the pointing accuracy requirement can be addressed by a closed loop Pointing, Acquisition, and Tracking (PAT) system incorporating the advanced attitude control system, host Attitude Determination, and Control System (ADCS), scanning mirror technologies, transmitter beam broadening, and position detectors (e.g. quadrant detectors) [28,29,35]. Fitting all the components of the omnidirectional transceiver in 1U is convenient but not mandatory for every application. Detail implementation techniques are subjective and can be accomplished in many ways based on the applications. In the design analysis, we opt for 850 nm as the operating wavelength to achieve less divergence, as well as the availability of low-cost Si APDs, high power lasers (e.g. VCSELs, semiconductor lasers), and COTS optics. All analyses are scalable to other wavelengths, such as conventional telecom wavelengths near 1550 nm with compatible component parameters. Most components are already available in space grade. With increasing demand, new components such as high-speed MEMS mirror are being tested for space applications.

CONCLUSION

Transmitter beam size optimization techniques possess the tradeoff among maximum achievable received power, host satellite vibration, and pointing precision requirement, the space-power limitations, component availability as well as the interplay between the beam divergence and scattering for a given distance. We present a systematic optical design optimization rule considering all the design variables mentioned above to pave the way to omnidirectional CubeSat crosslink based advanced applications.

ACKNOWLEDGMENTS

This work was supported by Small Spacecraft Technology Program, NASA: NNX16AT64A and Office of Naval Research, ONR N00014-18-1-2845. The authors would like to thank Dr. Rasul Torun for his valuable input to this work.

REFERENCES

[1] Selva D and Krejci D 2012 A survey and assessment of the capabilities of Cubesats for Earth observation Acta Astronautica 74 50–68

[2] Velazco J E, Griffin J, Wernicke D, Huleis J, DeNucci A, Boyraz O and Zaman I U 2018 Inter-satellite omnidirectional optical communicator for remote sensing CubeSats and NanoSats for Remote Sensing II CubeSats and NanoSats for Remote Sensing II vol 10769 (International Society for Optics and Photonics) p 107690L

[3] Peral E, Im E, Wye L, Lee S, Tanelli S, Rahmat-Samii Y, Horst S, Hoffman J, Yun S H, Imken T and Hawkins D 2018 Radar Technologies for Earth Remote Sensing From CubeSat Platforms Proceedings of the IEEE 106 404–18

[4] Devaraj K, Ligon M, Blossom E, Breu J, Klofas B, Colton K and Kingsbury R 2019 Planet High Speed Radio: Crossing Gbps from a 3U CubeSat Small Satellite Conference

[5] Leveque K, Carleton L, King J, Cuseo Z and Babb R 2019 Unlocking the Next Generation of Nano-Satellite Missions with 320 Mbps Ka-Band Downlink: On-Orbit Results Small Satellite Conference

[6] Farzana I.Khatri, Bryan S.Robinson, Marilyn D.Semprucci and Don M.Boroson 2015 Lunar Laser Communication Demonstration operationsarchitecture Acta Astronautica 111 77–83

[7] Velazco J E, Griffin J, Janzen A W, Huleis J, Peng M, DeNucci A, Zaman I U and Ozdal Boyraz 2018 High Data Rate Inter-Satellite

Omnidirectional Optical Communicator 32nd Annual AIAA/USU Conference on Small Satellites AIAA/USU Conference on Small Satellites pp SSC18-WKI-02

[8] Winker D M, Pelon J, Coakley J A, Ackerman S A, Charlson R J, Colarco P R, Flamant P, Fu Q, Hoff R M, Kittaka C, Kubar T L, Le Treut H, Mccormick M P, Mégie G, Poole L, Powell K, Trepte C, Vaughan M A and Wielicki B A 2010 The CALIPSO Mission Bull. Amer. Meteor. Soc. 91 1211–30

[9] Gentry B, McGill M, Schwemmer G, Hardesty M, Brewer A, Wilkerson T, Atlas R, Sirota M and Lindemann S 2006 THE TROPOSPHERIC WIND LIDAR TECHNOLOGY EXPERIMENT (TWiLiTE): AN AIRBORNE DIRECT DETECTION DOPPLER LIDAR INSTRUMENT DEVELOPMENT PROGRAM Earth Science Technology Conference

[10] Boroson D M, Robinson B S, Murphy D V, Burianek D A, Khatri F, Kovalik J M, Sodnik Z and Cornwell D M 2014 Overview and results of the Lunar Laser Communication Demonstration Free-Space Laser Communication and Atmospheric Propagation XXVI Free-Space Laser Communication and Atmospheric Propagation XXVI vol 8971 (International Society for Optics and Photonics) p 89710S

[11] Carrasco-Casado A, Takenaka H, Kolev D, Munemasa Y, Kunimori H, Suzuki K, Fuse T, Kubo-Oka T, Akioka M, Koyama Y and Toyoshima M 2017 LEO-to-ground optical communications using SOTA (Small Optical TrAnsponder) – Payload verification results and experiments on space quantum communications Acta Astronautica 139 377–84

[12] Fuchs C and Schmidt C 2019 Update on DLR's OSIRIS program International Conference on Space Optics — ICSO 2018 International Conference on Space Optics — ICSO 2018 vol 11180 (International Society for Optics and Photonics) p 111800I

[13] Tanaka T, Kawamura Y and Tanaka T 2015 Development and operations of nano-satellite FITSAT-1 (NIWAKA) Acta Astronautica 107 112–29

[14] Rose T S, Rowen D W, LaLumondiere S, Werner N I, Linares R, Faler A, Wicker J, Coffman C M, Maul G A, Chien D H, Utter A, Welle R P and Janson S W 2019 Optical communications downlink from a 1.5U Cubesat: OCSD program International Conference on Space Optics — ICSO 2018 International Conference on Space Optics — ICSO 2018 vol 11180 (International Society for Optics and Photonics) p 111800J

[15] Zaman I U, Janzen A W, Torun R, Peng M, Velazco J E and Boyraz O 2018 Omnidirectional optical transceiver design techniques for multi-frequency full duplex CubeSat data communication SPIE Optics and Photonics, CubeSats and NanoSats for Remote Sensing II (10769-42)

[16] Zaman I U, Janzen A W, Torun R, Velazco J E and Boyraz O 2018 Design Tradeoffs and Challenges of Omnidirectional Optical Antenna for High Speed, Long Range Inter CubeSat Data Communication Small Satellite Conference, Delivering Mission Success (SSC18-WKII-06)

[17] Technologies M 2017 Mirrorcle Technologies MEMS Mirrors - Technical Overview

[18] Optotune Dual axis VCM with position feedback2D Beam Steering

[19] Anthony E. Siegman LASERS (Sausalito, California: University Science Books) pp 665–72

[20] Guenther R D 1990 Modern Optics (John Wiley & Sons, Inc) pp 335–40

[21] International Telecommunication Union (ITU) 2000 G.975 : Forward error correction for submarine systems

[22] International Telecommunication Union (ITU) 2018 G.709.2 : OTU4 long-reach interface

[23] Micro Laser System Inc. Adjustable Fiber Collimators

[24] Thorlabs Collimation / Coupling

[25] Princetel FIBER COMPONENTS: Large-beam fiber collimators

[26] TAKENAKA H 2011 Link budget analysis for small optical transponder onboard small satellites Co61st International Astronautical Congress, Praguemmunication, 2010. Koetzting, Germany, May 16-20 1–8

[27] Chan V W S 2003 Optical satellite networks J. Lightwave Technol. 21 2811–27

[28] Kingsbury R W 2015 Optical communications for small satellites Thesis (Massachusetts Institute of Technology)

[29] Grenfell P, Aguilar A, Cahoy K and Long M Pointing, Acquisition, and Tracking for Small Satellite Laser Communications 7

[30] Ding Y, Nikitichev D I, Krestnikov I, Livshits D, Cataluna M A and Rafailov E U 2010 Quantum-dot external-cavity passively modelocked laser with high peak power and pulse energy Electronics Letters 46 1516–8

[31] Mayer A S, Phillips C R and Keller U 2017 Watt-level 10-gigahertz solid-state laser enabled by self-defocusing nonlinearities in an aperiodically poled crystal Nature Communications 8 1–8

[32] Ahmad F R and Rana F 2008 Passively Mode-Locked High-Power (210 mW) Semiconductor Lasers at 1.55-μm Wavelength IEEE Photonics Technology Letters 20 190–2

[33] Siegfried W Janson Cubesat-scale laser communications National Space Symposium, 2015

[34] Blue Canyon Technologies Components

[35] Chang J, Schieler C M, Riesing K M, Burnside J W, Aquino K and Robinson B S 2019 Body pointing, acquisition and tracking for small satellite laser communication Free-Space Laser Communications XXXI Free-Space Laser Communications XXXI vol 10910 (International Society for Optics and Photonics) p 109100P

Imam Uz Zaman is currently working toward his Ph.D. at the University of California, Irvine (UCI). He received his M.S. in Electrical Engineering from UCI in 2018 and his B.Sc. from the the Bangladesh University of Engineering and Technology (BUET). Zaman's research interests include designing analog optical link, free space miniature optical system development, CubeSat communication system, and laser remote sensing.

Dr. Velazco, the JPL principal investigator of this effort, has over 20 years of experience in carrying out R&D projects. For more than a decade Dr. Velazco worked on implementing wideband receivers for electronic surveillance applications including wide-open and superheterodyne receivers where he acquired expertise in direction-of-arrival (Direction Finding) hardware and software. Recently he worked on an advanced multimegabit Optical communicator for ground applications. Dr. Velazco is the technical supervisor of JPL's Applied Electromagnetic group.

Dr. Ozdal Boyraz is with the University of California, Irvine, where he is a Professor in the Department of Electrical Engineering and Computer Science. He works on integrated optics, optical communications systems, free space optical communication systems, active optical devices, and radiation detection. Up to date, he served as the PI or Co-PI of federally funded projects such as NASA Cube-Sat optical communicator, silicon and silicon nitride based optical devices, sensor and optomechanical devices.

Figure captions:

Fig. 12. CubeSat swarm interconnected by OOT.
Fig. 13. (a) A CubeSat omnidirectional optical communicator (b) The concept of 360° field of regard.
Fig. 14. Free space optical transmitter, (a) Galilean beam expander-based system and (b) Keplerian beam expander-based system.
Fig. 15. (a) Type A transmitter design, (b) the required ρ and TD for different scanning angles.
Fig. 16. Type B transmitter design in Zemax. All dimensions are in millimeters.
Fig. 17. Scanning area filling pattern (a) HFP, (b) SFP.
Fig. 18. CubeSat scanning area.
Fig. 8. Required mechanical small step angle of the scanning mirror. The solid lines are the nonlinear least- square fit on simulated data points.
Fig. 19. Scanning area filling efficiency for different initial beam sizes and small step angles.
Fig. 20. Effect of M_R on the beam size (solid curves) and peak irradiance (dashed curves) at 100 km.
Fig. 21. Effect of the mirror's instantaneous angle on the peak irradiance.
Fig.12. Effect of the relative receiver position from the transmit beam center on normalized received power.
Fig. 13. Effect of transmitter peak power on ECBW at different communication distances.